

CMB polarization with the Bicep and Keck experiments

Michael Crumrine

May 4, 2017

1 Introduction

1.1 A Brief History of Inflation

The modern study of cosmology began in 1915 with Einstein's development of the general theory of Relativity [7]. By combining the Einstein Field Equations with the assumptions of a homogeneous and isotropic universe, Friedmann developed a cosmological model which forms the core of the standard model of cosmology[8]. Hubble's observations in the 1930s showed an expanding universe[9] providing the first evidence for a Big Bang origin. This was further supported by the detection of the Cosmic Microwave Background by Penzias and Wilson in 1965[12].

Increasing experimental precision revealed a uniform CMB and isotropic universe on scales exceeding the size of the horizon predicted by Friedmann cosmological models. In 1981 Guth suggested a small period of exponential expansion to solve these two problems. This theory of inflation has since seen further success in explaining the growth of cosmic structures and the lack of observed magnetic monopoles but has been criticized due to its need for fine-tuned initial conditions.

1.2 Origins of the CMB

One of the most successful predictions of inflation is the presence of a near uniform isotropic photon source known as the Cosmic Microwave Background (CMB). The CMB has the near uniform temperature spectrum of a 2.73K blackbody and is the source of the oldest photons in the universe. In the hot big bang, the early universe was an energetic plasma in which photons scattered continuously from free protons and electrons which prevented propagation over large distances. As the universe expanded, the temperature of this plasma decreased adiabatically until the free electrons and protons could combine to form neutral Hydrogen. After this era of recombination about 380,000 years after the big bang, the photons decoupled from the plasma and began free streaming through the universe, redshifting due to continued expansion. We observe these photons as a 2D "surface of last scattering".

2 Science with the CMB

2.1 Mapping the CMB

Precision cosmology experiments have shown that the CMB is not truly uniform. Results from COBE in 1992[5] showed the CMB to have a nearly isotropic temperature spectrum corresponding to a 2.73K blackbody but with fluctuations on the order of $10 \mu\text{K}$. We examine these temperature perturbations with the spherical harmonics:

$$\delta T(\theta, \phi) = \sum_{m=-\ell}^{\ell} \sum_{\ell=0}^{\infty} a_{\ell m} Y_{\ell m}(\theta, \phi) \quad (1)$$

Although this decomposition is a powerful tool, the universe is isotropic only in a statistical sense and we therefore cannot predict any individual $a_{\ell m}$. We instead take an average over m for a given ℓ to form the angular power spectrum:

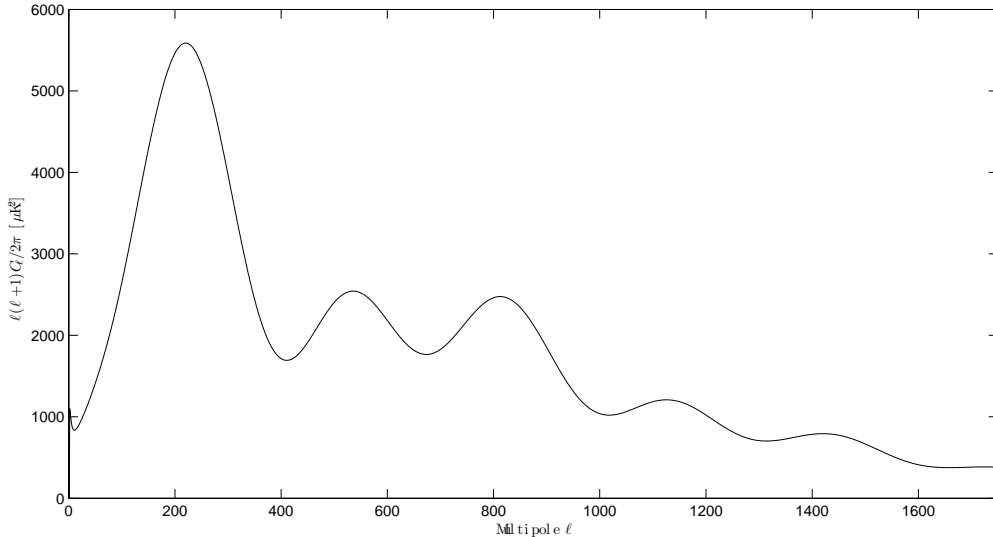


Figure 1: The temperature power spectrum of the CMB. The primary and acoustic peaks can be used to constrain cosmological parameters that describe the geometry, evolution and composition of our universe.

$$C_\ell = \frac{1}{2\ell + 1} \sum_{m=-\ell}^{\ell} |a_{\ell m}|^2 \quad (2)$$

The temperature power spectrum shown in Figure 1 contains much of the information concerning the geometry, evolution, and composition of our universe.

2.2 Polarization Anisotropies

In addition to the temperature anisotropies CMB photons are partially polarized due to Thompson scattering in a non-uniform temperature field. This CMB polarization was predicted at the $\approx 10\%$ level by Bond et al [6] and first detected by DASI in 2002 [11]. Polnarev [16] realized that an inflationary period would imprint an additional polarization signal on the CMB due to the production of gravitational waves.

This inflationary gravitational wave (IGW) signal is expected to be orders of magnitude fainter than the signal due to Thompson scattering and difficult to separate in the Stokes parameter space conventionally used when studying linearly polarized light. It was shown by

Kamionkowski et al [10] that the polarization could instead be parameterized by a gradient (E-mode) and curl (B-mode) component. The signal produced by Thompson scattering occurs in the presence of a temperature quadrupole and follows the temperature gradients of the hot plasma at recombination. It can therefore produce only E-modes. The tensor perturbations due to passing gravitational waves are not restricted in this way and can thus generate both E and B modes. The signal produced by these two methods is characterised by the tensor to scalar ration r .

In addition to the temperature power spectrum, we can then examine the E, B power spectrum as well as cross correlations between the temperature and polarization power spectra. Figure 2 shows the theoretical power spectra of CMB perturbations in the Λ CDM standard model of Cosmology with the addition of an $r = 0.1$ IGW B-mode signal.

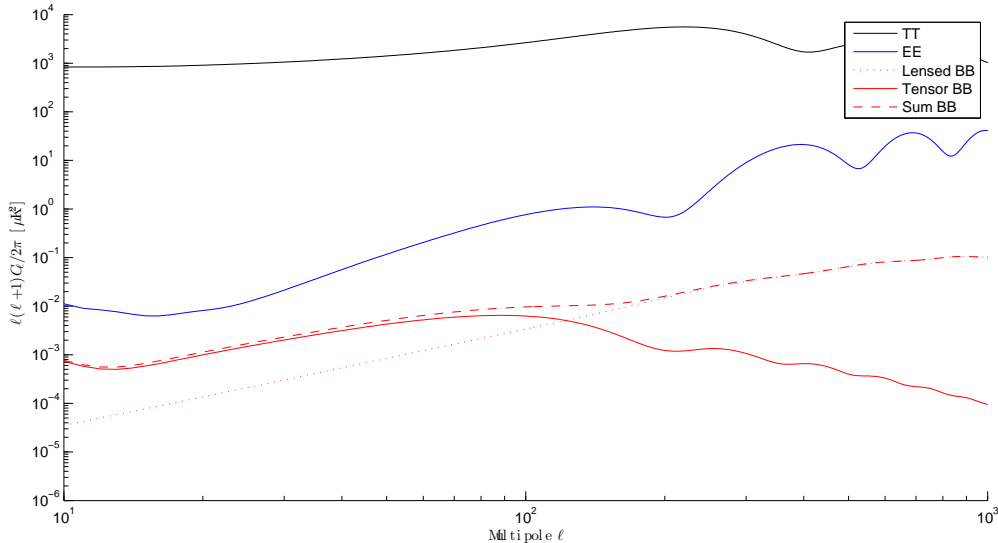


Figure 2: The CMB power spectrum of the Λ CDM standard model of cosmology as calculated by CAMB using parameters from Planck 2013. The temperature anisotropies (black) contain orders of magnitude more power than the E-mode (blue) and B-mode (red) polarization anisotropies. The BB spectrum is split into a lensing component (dotted) and a tensor component (solid) plotted at the $r = 0.1$ level.

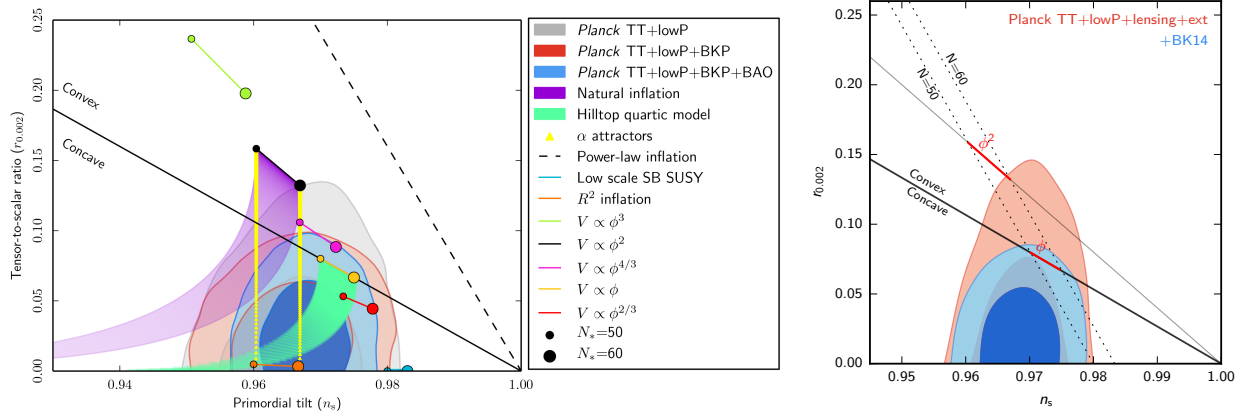


Figure 3: Left: Reproduced from Planck 2015 XX: "Constraints on Inflation" [15] shows theoretical predictions for select inflationary models in the n_s, r parameter space and current constraints on those parameters. The two dots correspond to different numbers of e-folds. Right: Reproduced from BK-VI [3] showing improved constraints in this parameter space from the latest Bicep / Keck data including a 95GHz band.

2.3 Constraints on Inflation

Although the theory of inflation provides an attractive solution to a number of problems with the standard big bang cosmology, the exact physics of inflation are still undetermined. The favored theory of slow roll inflation proposes a scalar field ϕ in which the potential of the field dominates over its kinetic energy. There are many possible potentials which fit the mathematical requirements of inflation theory which yield a range of values for the tensor to scalar ratio. By continuing to push the constraints on r we restrict the possible potentials of this scalar field. A summary of current restrictions on r and n_s which depends on the slow roll parameters is shown in Figure 3. The Bicep / Keck constraints heavily disfavor the ϕ^2 model but still allow for other models which have $r < 0.1$.

3 The Bicep and Keck Program

The Bicep/Keck experiments are a staged series of small aperture ground based telescopes which aim to produce extremely deep degree-scale polarization maps of the CMB. The high systematics control and long integration time have enabled Bicep and Keck to set the strictest

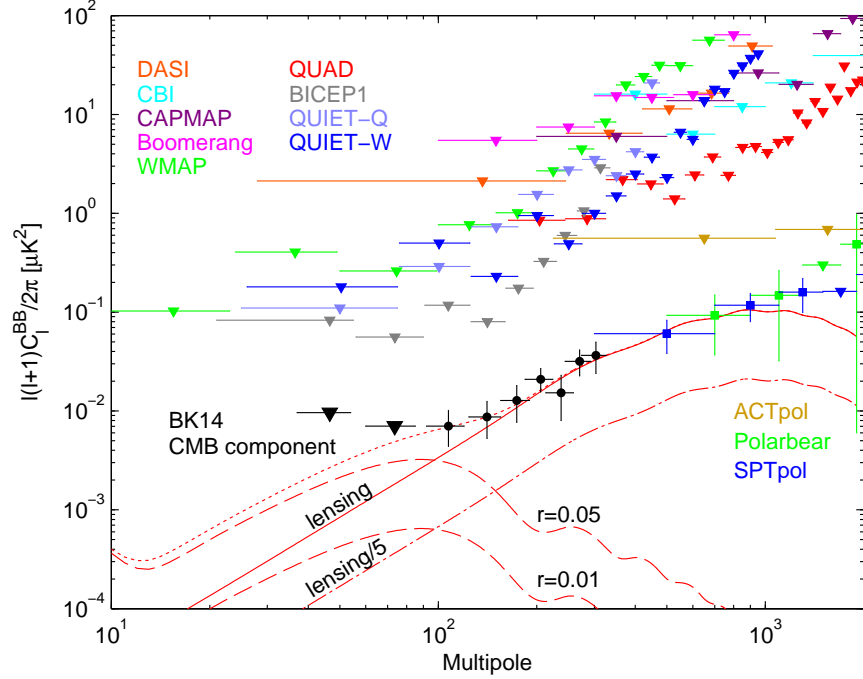


Figure 4: Published B-mode polarization measurements of the CMB. Theoretical predictions for lensing B-modes (solid red) and IGW B-modes (dashed red) for two values of r are shown. The SPTpol, Polarbear and Bicep/Keck experiments have all recently detected the B-mode lensing signal. Bicep and Keck are currently alone in probing large angular scales for the IGW B-mode signal

limits on inflationary gravitational wave B-mode signal to date. Current published B-mode measurements are shown in Figure 4.

Each generation of receiver builds on the experience gained from the previous generation while pushing deeper in sensitivity. Bicep1 was deployed to the south pole in 2006 and used 98 feedhorn coupled bolometers observing at 100GHz and 150GHz. Over three observing seasons the strategies developed for observation, calibration and systematics control proved the efficacy of small aperture refractors for CMB polarization studies and established the leading upper bounds on inflation at $r < 0.70$ [1].

Building on the techniques developed with its predecessor, Bicep2 replaced Bicep1 in 2009. It exchanged feedhorn coupled bolometers for antenna-coupled transition edge sensor (TES) bolometer arrays developed at JPL which have been used in every subsequent telescope in the series. Concentrating its observing power at 150GHz, in March 2014 Bicep2

announced a detection of excess signal in its observing band consistent with an IGW signal of $r = 0.2$ [2]. However, the interpretation of this excess as IGW signal relied heavily on models of polarized dust emission which had not been highly constrained at the time. Later that year new high frequency maps from the Planck experiment indicated that the dust models had underestimated polarized emission in the faintest sky regions [13]. A joint analysis with Planck and cross correlation between the Planck 353GHz and Bicep2 150GHz maps showed that a substantial part of the observed excess in Bicep2 was due to polarized dust emissions [4]. This joint analysis established a new upper limit of $r < 0.12$

The Keck Array deployed to the south pole in 2012 with five 150GHz receivers similar to Bicep2. These additional receivers confirmed the excess signal found with Bicep2 and contributed to the March 2014 results. In addition to extending the Bicep2 survey depth at 150GHz the Keck array has extended observations into three other observing bands at 95GHz, 220GHz and 270GHz. The extension into other frequencies harnesses the Bicep/Keck program's proven capability to make deep maps to further constrain galactic foregrounds and refine the models of polarized dust emission. The Keck array is in its final observing season with four receivers in the 220GHz band and one at 270GHz.

In the fall of 2014 Bicep3 was deployed at the south pole to run concurrently with the Keck array. Bicep3 vastly expands the design of the Bicep2 instrument with a focal plane containing 2500 detectors in the 95GHz band, almost 10x the 288 detectors of a Keck style 95GHz receiver. Bicep3 serves as our prototype instrument leading to the eventual replacement of the Keck array with Bicep array.

The Bicep array is a funded experiment which will replace the Keck Array for multifrequency observations. Using the more powerful Bicep3 style receivers, Bicep array will field three receivers centered at 35GHz, 95GHz, and 150GHz along with a dual band 220/270GHz receiver. The new 35GHz receiver will heavily constrain galactic synchrotron radiation past the upper limits set by WMAP's 23GHz band while the increased sensitivity at higher fre-

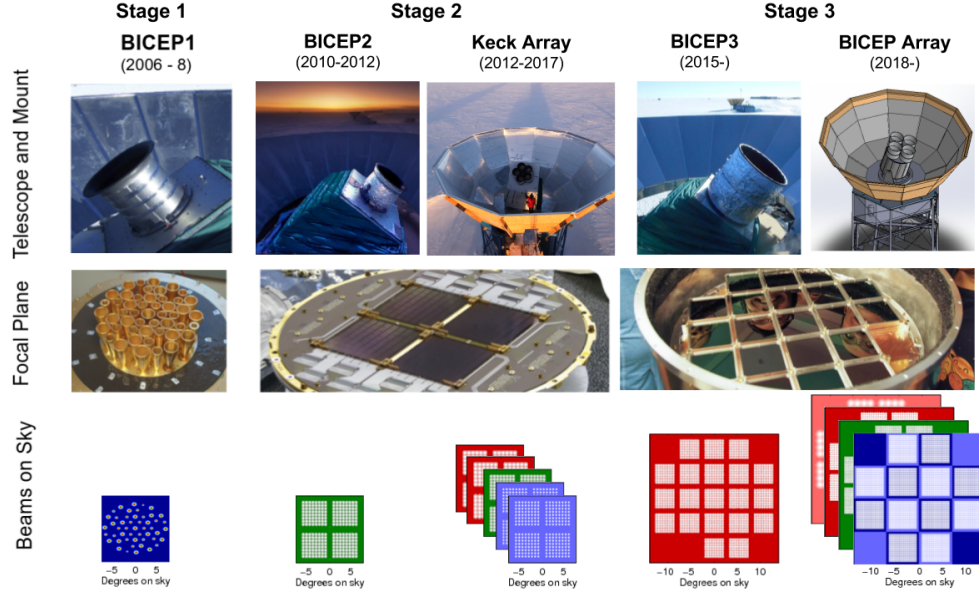


Figure 5: The progression of the Bicep/Keck program from Bicep1 to Bicep Array. The bottom row shows the beam patterns of the focal planes on the sky. With the exception of Bicep1 the focal plane colors correspond to band centers of: 35GHz - pink, 95GHz - red, 150GHz - green, 220 GHz - light blue, 270GHz - dark blue.

quencies will allow for better constraints on dust emissions at frequencies closer to our other bands than the Planck 353GHz data.

4 Multifrequency Observations

CMB polarization experiments must be able to separate polarized foreground signals from those imprinted on the CMB. Although these signals can be minimized by selection of observing area their emissions must be constrained and accounted for. As shown by the 2014 joint analysis between Bicep2/Keck and Planck, constraints on these models have significant impact on the interpretation of any observed excess signal. By expanding observations into multiple frequencies, the Keck array has further constrained these dust emissions as well as emissions due to galactic synchrotron as shown in Figure 6.

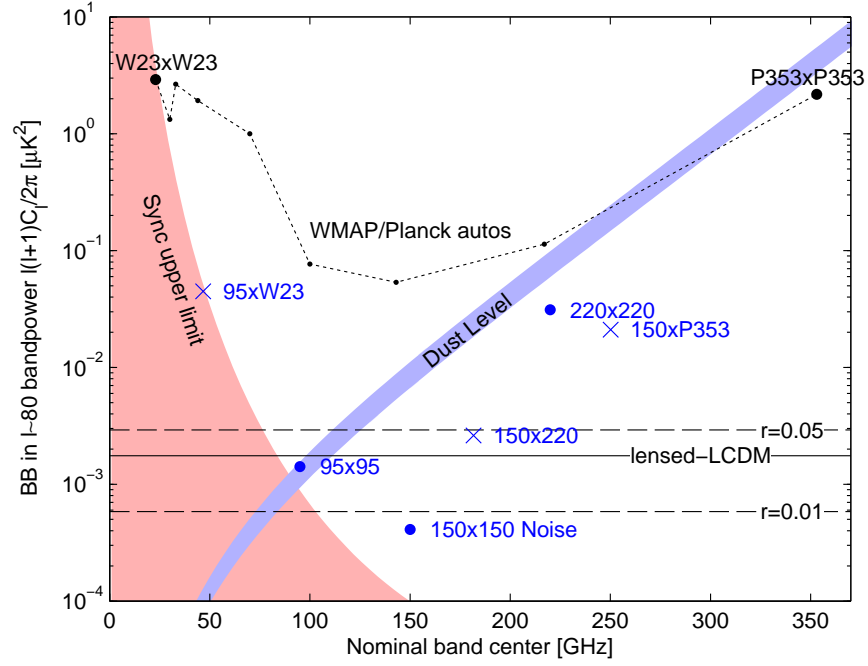


Figure 6: Noise levels in the Bicep/Keck combined observations through the 2015 observing season. The shaded regions show constraints on the signal level of galactic foregrounds and signal levels corresponding to select values of r are shown at the bottom. All values are shown in the $\ell = 80$ bandpower where the IGW signal is expected to be maximal.

4.1 Polarized Dust

Polarized emissions from galactic dust provide an excess BB signal on top of that expected from Λ CDM and gravitational lensing which (although low in power) are significant compared to the IGW signal. These emissions depend significantly on frequency, exhibiting a power law like dependence. As shown in Planck XXII [14] the spectral energy distribution of galactic dust can be described by a modified blackbody spectrum

$$I_d = A_d \nu^{\beta_d} B_{\nu}(T_d) \quad (3)$$

Where A_d is an amplitude at some frequency and $\beta_d > 0$ is the spectral index of dust emission and $B(T)$ is the standard blackbody spectrum. In order to fully constrain the dust signal we must complement this intensity spectrum with a description of the dust's spatial behavior

$$D_{\ell} \propto \ell^{\alpha} \quad (4)$$

where $D_{\ell} = C_{\ell} \frac{\ell(\ell+1)}{2\pi}$. The parameters in these equations model the dust contribution to polarization signal in our field. As Equation 3 shows this signal is brighter at higher frequencies. We therefore use the Planck 353GHz maps to set these dust parameters and extrapolate to our observed frequencies. This necessarily means that any uncertainty contained in the high frequency observations is magnified due to the power law behavior.

Figure 6 shows the noise uncertainty and signal levels the $\ell = 80$ bandpower where the IGW signal is expected to peak. The low 150x150 noise allows us to detect excess signal with high significance. However, the high P353xP353 noise as compared to dust signal does not provide significant enough constraining power to separate dust signal from potential IGW signal in the 150GHz band. The 220x220 point shows preliminary numbers from our 2015 observing season in which the Keck array operated with two 220GHz receivers and

provides similar constraining power to the Planck 353GHz data while being closer to our main observing bands. Two additional 220GHz receivers were added for the 2016 observing season and observations at 270GHz will begin in the current 2017 season. These observations will allow us to produce continually improving constraints on dust in our field.

4.2 Galactic Synchrotron

An upper limit for an additional foreground signal is shown in Figure 6. Rather than increasing in intensity at higher frequencies, polarized emissions from galactic synchrotron radiation are strongest at low frequencies. We model synchrotron emission intensity as

$$I_\nu = A_s \nu^{\beta_s} \quad (5)$$

where $\beta_s < 0$ describes the fall off in intensity with frequency and A_s is the amplitude. The angular power spectrum of galactic synchrotron follows the same form as dust (Equation 4). The points shown in Figure 6 mark the upper limit of synchrotron emissions as the noise level of current observations in these bands is not sufficient for detection. Models of the contribution due to synchrotron do not predict significant contamination at frequencies upwards of 150GHz due to the strong frequency dependence.

5 Bicep Array

5.1 Experiment Overview

Bicep Array will deploy four Bicep3 style receivers in four frequency bands with first light expected in 2019. Building on the success of previous experiments, Bicep Array will continue to use the antenna coupled transition edge sensor (TES) bolometers developed by JPL. These detectors leverage the strong temperature-dependence of superconductors near their

transition point to detect extremely faint signals. The signal from these bolometers is then amplified by a series array of superconducting quantum interference devices (SQUIDs). We use cold optics to minimize the out of band extraneous signal incident on our detectors.

Each Bicep array receiver will field ≈ 10 time the detectors of a Keck receiver in the same band. The additional increase in aperture from 26cm to 55cm will quickly push sensitivity to synchrotron with Bicep Array's new band and continue to push sensitivity in our deepest 95GHz and 150GHz bands. Projections for the sensitivity of the Bicep / Keck experiments including the Bicep array are shown in Figure 7. As we continue to increase in sensitivity to r , the B-mode lensing component will become a significant contributor to σ_r . This achromatic foreground cannot be constrained with multifrequency observations but it can be accounted for via delensing. Given a high resolution map of the angular deflection field $\Delta\phi$ of the CMB photons from last scattering to observation it is possible to undeflect Stokes Q, U maps of polarized signal. The third generation SPT-3G receiver deployed to the South Pole in late 2016 and will spend a significant fraction of their time observing the Bicep/Keck sky patch. Using ϕ and Q/U maps provided by SPT-3G will allow us to push σ_r below 0.005.

5.2 Cryogenic Considerations

The cryogenic operating temperatures of our detector and optics system require a specially designed housing to thermally isolate the focal plane as much as possible. As with Keck and Bicep3 the Bicep Array cryostats will consist of a nested ambient temperature vacuum jacket, a 50K radiation shield, and a 4K optics tube. This nested approach protects the low temperature optics from absorbing significant radiative power since $P \propto (T_H^4 - T_C^4)$. In addition to radiation shielding, there is an additional trade-off between structural support and heat conduction between the temperature shells. A low conductive loading may introduce significant deviation in pointing direction while more structural supports increase the thermal load on the cooling system.

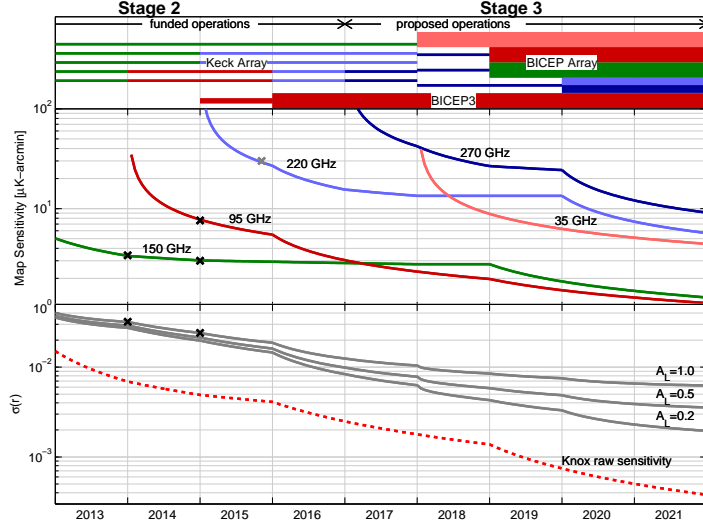


Figure 7: Projected sensitivity of the ongoing and planned Bicep/Keck observational program. The increased throughput of the Bicep array receivers will provide increased sensitivity and continue to constrain inflation at a rapid rate. *Note: Projections are directly scaled from published results and thus include real-world inefficiencies that are not reflected in purely theoretical projections. X's mark sensitivities achieved in BKP and BK-VI [3, 4].* Middle: Map depth at each frequency as a function of time. Bottom: Sensitivity to r for selected levels of delensing efficiency. Performance between $A_L = [0.2, 0.5]$ is expected.

5.3 Thermal Loading

The cryostat is operated at high vacuum ($\approx 10^{-5}$ mTorr) which largely eliminates conductive loading due to residual gasses. The two largest contributions are due to conduction across the structural supports and radiation from higher temperature stages. Of these, the radiation absorbed by the lower temperature shells has the highest possible contribution. Radiative heat transfer for cryogenic systems is a well studied subject. We follow Ekin's textbook on cryogenic engineering to estimate this thermal load according to:

$$\dot{Q}_{h \rightarrow c} = \sigma A_c E (T_h^4 - T_c^4) \quad (6)$$

where the h and c subscripts denote the hot and cold surfaces respectively, and E depends on the emissivity of the surfaces as

Material	Emissivity
Rough Aluminum	$\epsilon = 0.07 - 0.1$
Polished Aluminum	$\epsilon = 0.04 - 0.06$
Aluminized Mylar	$\epsilon = 0.035$
OFHC Copper	$\epsilon = 0.65$

Table 1: Typical emissivity values for materials used in the construction of the Bicep Array cryostats.

$$E = \frac{1}{1/\epsilon_h + 1/\epsilon_c - 1} \quad (7)$$

Equation 6 is valid for parallel plates, and concentric cylinders assuming specular reflection regime. Table 1 shows typical emissivities for the materials used in the Bicep Array cryostats. In addition to the radiative load, the structural supports conduct heat between the temperature shells according to the Fourier heat transfer law:

$$\dot{Q}_{1 \rightarrow 2} = \int_{T_1}^{T_2} \frac{A}{L} K(T) dT \quad (8)$$

The large temperature change across the support struts require a detailed knowledge of how the materials' thermal conductivity changes with temperature. NIST has a collection of thermal conductivity measurements for commonly used materials in cryogenic design including Aluminum and Titanium. Bicep Array uses six Titanium “V” shaped supports at the front end to keep the optics tube centered and six carbon fiber struts at the back end which support most of the weight. Carbon fiber as a material is non-standardized which makes determining the thermal properties difficult, especially at high temperatures where few conductivity measurements exist. We therefore supplement published low temperature measurements with direct measurements of conducted power in a test cryostat system.

5.4 Radiation Shielding

The large surface area of the 50K radiation shield absorbs a significant amount of radiation. Using Equation 6 the raw radiated heat transfer to the 50K shell from the enclosing 300K vacuum jacket is 107W which is far outside the capacity of our first stage pulse tube cooling system. To reduce this load we surround the lower temperature shell with a series of thermally floating layers of Aluminiz Mylar. This Multiple Layer Insulation (MLI) creates a temperature gradient of isolated radiating shells which significantly reduces the transmitted power by reducing the $\Delta(T^4)$ term of Equation 6. The modified power transmission to the cold shell when shielded by N layers of MLI is

$$\dot{Q}_{h \rightarrow c} = \frac{\sigma A_c (T_h^4 - T_c^4)}{1/\epsilon_h + 1/\epsilon_c - 1 + N(2/\epsilon_m - 1)} \quad (9)$$

where ϵ_m is the emissivity of the MLI. Placing 30 thermally floating layers in between the 300K vacuum shell and the 50K radiation shield reduces absorbed radiative power to 2.73W at which point it becomes subdominant to the thermal loading from the structural supports and the absorptive optical filters. Although the radiation absorbed by the 4K stage from the 50K stage is much lower due to the smaller $\Delta(T^4)$ we choose to include 5 layers of MLI between the 50K radiation shield and the 4K optics tube as well.

5.5 Thermal Loading and Implications for Pointing

Using the equations above we can estimate the thermal loading on each of the two cryogenic stages of the cryostat and estimate an operating temperature for both stages of our pulse tube cooling system. We require a 4K stage operating temperature of less than $\approx 3.5K$ to allow the second stage He fridge to function. The 50K stage operating temperature is not as crucial, however lower temperatures allow for cooler optical filters which then radiate less power directly down the optics tube. Using equations 8 and 9 we calculate the thermal load

	50K	4k
Radiation	$2.73W$	$0.0479W$
Bottom Supports	$< 2.4W$	$0.0759W$
Top Supports	$1.93W$	$0.0821W$
Data Cables	$1.07W$	$0.05W$
Optical Filters	$12.51W$	$0.1538W$
<i>Total</i>	$20.64W$	$0.4097W$

Figure 8: Above we show the calculated thermal load on the 50K radiation shield and the 4K optics tube due to radiation from higher temperature stages, conduction across the structural supports, conduction across the data cables and radiation absorbed by the optical filters.

onto the 4K and 50K stages as shown below in Table 8.

In addition to the thermal load due to radiation from higher temperature stages and conduction across the structural supports we also account for conduction across the data cables which read out our detectors and the radiation absorbed by our optical filters at each stage. The thermal load due to the optical filters is obtained using data from the Bicep3 experiment’s actual performance. We expect similar performance from Bicep Array which shares the same aperture size and filtering scheme as Bicep3.

Using these numbers we can estimate the operating temperature of our pulse tube system by comparing the thermal load with the capacity curve supplied by the manufacturer shown in Figure 9. The calculated thermal load suggests a first stage operating temperature of 39K and a second stage temperature of 3.2K. While this is sufficient for operation, there is not much margin. We note however that the Bicep3 pulsetube significantly outperforms this Cryomech standard by $\approx 50\%$ on the first stage. This extra cooling capacity will help to alleviate some of the loading onto the optics stage by reducing the temperature gradients.

5.6 Implications for Pointing

The thermal load is closely tied to the pointing accuracy of the receiver. Table 8 shows that heat conduction across the supports is subdominant only to the thermal load from the optical filters. However, if we wish to reduce the conductive load across these supports it comes

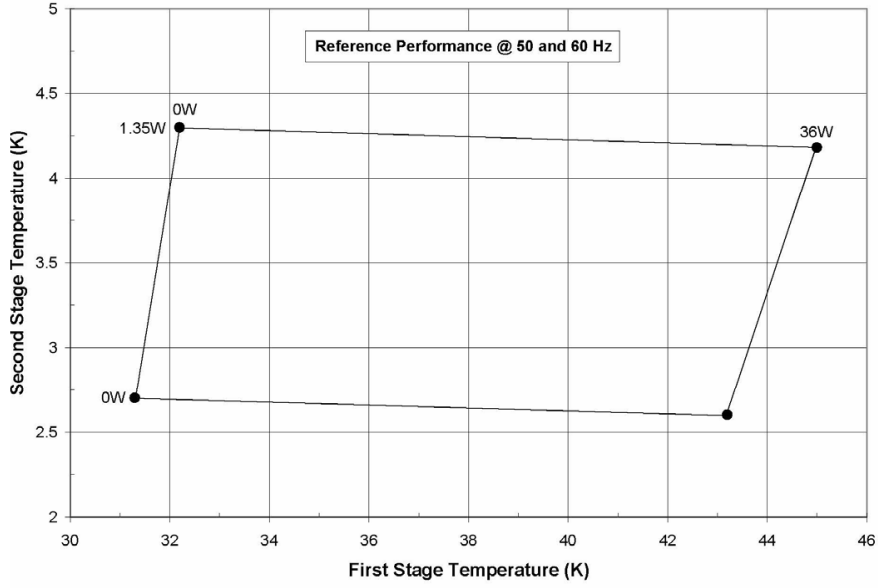


Figure 9: Reference capacity curve for the PT415 Pulse Tube Cryocooler with remote motor option as supplied by Cryomech. Using the estimated thermal load from Table 8 gives an operating temperature of 39K for the first stage and 3.2K for the second stage. The Bicep3 pulse tube is observed to significantly outperform the Cryomech standard

at the cost of a less rigid support system. To estimate the pointing accuracy of our optics tube, we use Finite Element Analysis to simulate the deformations of the cryostat under gravitational load. Figure 10 shows the results of a structural simulation performed with the COMSOL Multiphysics software suite. In this simulation the cryostat is rotated to our lowest observing elevation of 45 degrees and the gravitational load of all interior components are attached to their respective mounting surfaces.

We are most interested in the deformations of the cryostat in the direction perpendicular to the optical axis. This will give an indication of the shift in pointing of the optics tube with respect to the fixed outer vacuum jacket. A simple calculation of the deflection of the back of the optics tube with respect to the front yields a pointing shift of 10 arcseconds along the tube's 1.65m length. As a secondary check, we also fit a plane to three points on the deformed baseplate and calculate the angle of the surface normal to be 45.0028 degrees corresponding to a 10.255 arcsecond pointing shift. The detectors used in Bicep Array will have large

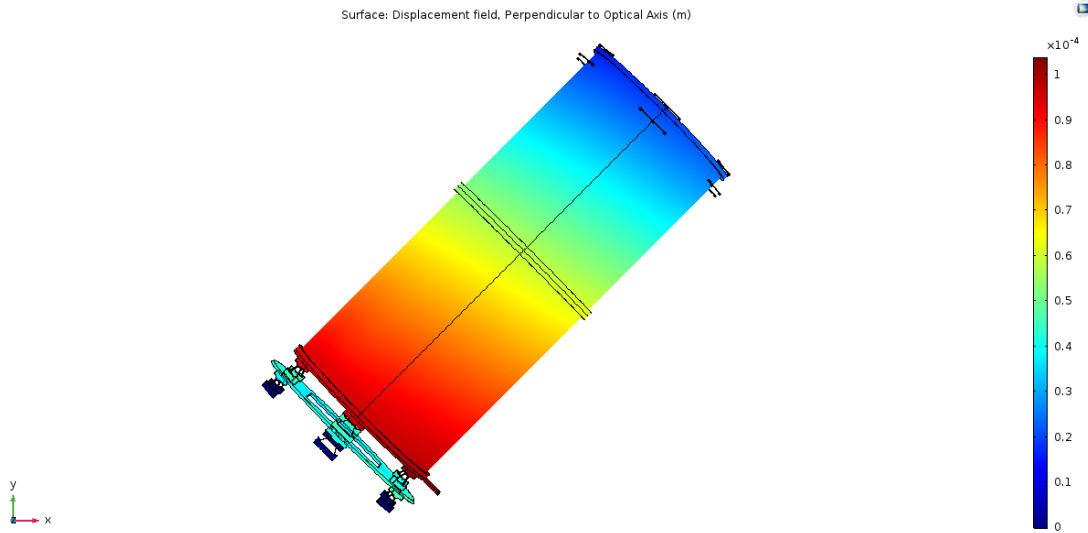


Figure 10: Simulation results of the deformation of the 4K optics tube under gravitational load as calculated by the COMSOL simulation suite. The colorscale shows the magnitude of deformation in the vector direction perpendicular to the optical axis (ie: -45 degrees). The deflections of the 50K radiation shield to which the 4K optics tube is attached are included in this simulation, however the shield is hidden for clarity.

beam sizes compared to this shift with the 270GHz detectors having the smallest beams of 9 arcmin FWHM. This pointing shift is then acceptable for the Bicep array experiment.

6 Conclusions

The Bicep Array experiment will continue the successful achievements of its predecessors by pursuing increasingly deep maps of the polarized component of the CMB and expanding these observations into other frequencies in order to constrain galactic foregrounds. The design of the cryostat is nearing completion and delivery of the first receiver is expected during the fall of 2017. After careful integration and characterization of the detectors and readout systems Bicep Array will deploy its first receiver to the South Pole in the winter of 2018. With a dual band 35/40 GHz focal plane this first receiver will rapidly push down the upper limits on polarized emission from galactic synchrotron. Future receivers will continue to push sensitivity in the bands at which Bicep / Keck have the deepest maps and at which

contribution from galactic foregrounds are dimmest. With delensing in conjunction with SPT-3G we expect to reach a sensitivity of $\sigma_r < 0.005$ by the end of the decade. This will place significant constraints on inflationary models and the dynamics of the universe's evolution within the first instants after the big bang.

References

- [1] D. Barkats et al. “Degree-scale Cosmic Microwave Background Polarization Measurements from Three Years of BICEP1 Data”. In: *apj* 783, 67 (Mar. 2014), p. 67. DOI: 10.1088/0004-637X/783/2/67. arXiv: 1310.1422.
- [2] BICEP2 Collaboration et al. “Detection of B-Mode Polarization at Degree Angular Scales by BICEP2”. In: *Physical Review Letters* 112.24, 241101 (June 2014), p. 241101. DOI: 10.1103/PhysRevLett.112.241101. arXiv: 1403.3985.
- [3] BICEP2 Collaboration et al. “Improved Constraints on Cosmology and Foregrounds from BICEP2 and Keck Array Cosmic Microwave Background Data with Inclusion of 95 GHz Band”. In: *Physical Review Letters* 116.3, 031302 (Jan. 2016), p. 031302. DOI: 10.1103/PhysRevLett.116.031302. arXiv: 1510.09217.
- [4] BICEP2/Keck and Planck Collaborations et al. “Joint Analysis of BICEP2/Keck Array and Planck Data”. In: *Physical Review Letters* 114.10, 101301 (Mar. 2015), p. 101301. DOI: 10.1103/PhysRevLett.114.101301. arXiv: 1502.00612.
- [5] N. W. Boggess et al. “The COBE mission - Its design and performance two years after launch”. In: *apj* 397 (Oct. 1992), pp. 420–429. DOI: 10.1086/171797.
- [6] J. R. Bond and G. Efstathiou. “Cosmic background radiation anisotropies in universes dominated by nonbaryonic dark matter”. In: *apjl* 285 (Oct. 1984), pp. L45–L48. DOI: 10.1086/184362.

- [7] A. Einstein. “Die Feldgleichungen der Gravitation”. In: *Sitzungsberichte der Königlich Preußischen Akademie der Wissenschaften (Berlin)*, Seite 844-847. (1915).
- [8] A. Friedmann. “Über die Krümmung des Raumes”. In: *Zeitschrift für Physik* 10 (1922), pp. 377–386. DOI: 10.1007/BF01332580.
- [9] E. Hubble. “A Relation between Distance and Radial Velocity among Extra-Galactic Nebulae”. In: *Proceedings of the National Academy of Science* 15 (Mar. 1929), pp. 168–173. DOI: 10.1073/pnas.15.3.168.
- [10] M. Kamionkowski, A. Kosowsky, and A. Stebbins. “A Probe of Primordial Gravity Waves and Vorticity”. In: *Physical Review Letters* 78 (Mar. 1997), pp. 2058–2061. DOI: 10.1103/PhysRevLett.78.2058. eprint: astro-ph/9609132.
- [11] J. M. Kovac et al. “Detection of polarization in the cosmic microwave background using DASI”. In: *nat* 420 (Dec. 2002), pp. 772–787. DOI: 10.1038/nature01269. eprint: astro-ph/0209478.
- [12] A. A. Penzias and R. W. Wilson. “A Measurement of Excess Antenna Temperature at 4080 Mc/s.” In: *apj* 142 (July 1965), pp. 419–421. DOI: 10.1086/148307.
- [13] Planck Collaboration et al. “Planck intermediate results. XIX. An overview of the polarized thermal emission from Galactic dust”. In: *aap* 576, A104 (Apr. 2015), A104. DOI: 10.1051/0004-6361/201424082. arXiv: 1405.0871.
- [14] Planck Collaboration et al. “Planck intermediate results. XXII. Frequency dependence of thermal emission from Galactic dust in intensity and polarization”. In: *aap* 576, A107 (Apr. 2015), A107. DOI: 10.1051/0004-6361/201424088. arXiv: 1405.0874.
- [15] Planck Collaboration et al. “Planck 2015 results. XX. Constraints on inflation”. In: *aap* 594, A20 (Sept. 2016), A20. DOI: 10.1051/0004-6361/201525898. arXiv: 1502.02114.

- [16] A. G. Polnarev. “Polarization and anisotropy induced in the microwave background by cosmological gravitational waves”. In: *azh* 62 (Dec. 1985), pp. 1041–1052.